# Nonequilibrium spatiotemporal dynamics of the Wigner distributions in broad-area semiconductor lasers

E. Gehrig[1,2] and O. Hess[1,*]
[1]*Theoretical Quantum Electronics, Institute of Technical Physics, DLR, Pfaffenwaldring 38-40, D-70569 Stuttgart, Germany*
[2]*Fachbereich Physik, University of Kaiserslautern, D-67663 Kaiserlautern, Germany*
(Received 5 September 1997)

We investigate the coupled microscopic and macroscopic nonequilibrium spatiotemporal dynamics of broad-area semiconductor lasers. Characteristic nonequilibrium Wigner distributions of the charge carriers and the interband polarization reveal spatially inhomogeneous field-induced heating and cooling as a consequence of the coupling of the optical field to the carrier and phononic systems. The numerical simulations are performed on the basis of microscopic spatially resolved Maxwell-Bloch equations in which the spatiotemporal variation of thermal properties of the active laser medium are self-consistently included. In particular, the spatiotemporal light-matter interactions are determined by the temporal and spatial transport of the electron-hole plasma, its dependence on carrier-carrier, carrier-phonon, and phonon-phonon scattering processes as well as on the optical properties and macroscopic boundary conditions. In resonantly and nonresonantly excited broad-area semiconductor lasers, the microscopically computed Wigner distributions of the charge carriers and the interband polarization reveal the spatiospectral dependence of the laser gain, the induced refractive index, as well as the electron and hole plasma temperatures. The spatiotemporal nature of these processes explains macroscopic effects such as dynamic thermal lensing and formation of spatiospectral optical structures. [S1050-2947(98)06503-2]

PACS number(s): 42.55.Px, 42.65.Sf, 78.20.Bh

## I. INTRODUCTION

Ever since its conception over 30 years ago, the semiconductor laser has been both in the interest of technology and at the forefront of fundamental research. Due to their small size and unrivalled high efficiency in transforming electrical energy into coherent light, semiconductor lasers are today's most widely used laser systems. However, when one seeks to increase the optical output power of a semiconductor laser by enlarging its active zone or by an integration of several lasers into an array, severe nonlinearities and instabilities emerge [1,2]. These effects continue to have detrimental influence on beam quality and spectral characteristics when compared to single-stripe semiconductor lasers with moderate output power. Recently, it has been theoretically predicted [3–5] and subsequently experimentally observed [6] that it is the combination of microscopic and macroscopic temporal and spatial dynamics which characterizes this behavior. A theoretical investigation consequently has to include both macroscopic external constraints imposed by a specific type of laser structure and a spatially resolved microscopic description of the interaction between the optical field and the active semiconductor medium.

In most theoretical descriptions, however, the characteristic semiconductor properties associated with the wave number dependence of the gain function, the induced refractive index distribution, etc. are described on the basis of phenomenological two-level approximations [7–9]. Thereby, both spatial variations and the spectral dependence represented by the semiconductor band structure are disregarded. Moreover, a characteristic feature of a semiconductor as the active medium of a laser is the fact that, besides the interaction with the light field, other types of interactions play an important role. These are, in particular, the Coulomb interaction among the carriers giving rise to many-body renormalizations, screening, and a thermalization of the nonequilibrium carrier distribution, as well as the interaction with phonons leading to an energy exchange between the carriers and the crystal lattice. To include these effects in a theoretical description of spatially resolved semiconductor lasers we have recently derived Maxwell-Bloch equations for spatially inhomogeneous semiconductor lasers which include both space dependence and momentum dependence of the charge carrier distributions and the polarization [4].

The nonequilibrium dynamics of semiconductor lasers have been the focus of a number of recent publications. They, however, have been performed mostly either on the basis of spatially homogeneous models [10] or, in the case of analyzing nonequilibrium dynamics due to pulse propagation in semiconductor amplifiers, by disregarding effects of counterpropagation and the transverse dependence of the optical fields [11,12]. Another shortcoming in the modeling of optical excitation of semiconductor laser structures is related to the specific form of the initial conditions entering into the numerical simulation scheme. Furthermore, in the simulations one frequently assumes nonequilibrium initial conditions for the distribution functions and, e.g., subsequently analyzes their relaxation [13,14]. Clearly, a more realistic way would be to treat in the simulation both the way nonequilibrium carrier distributions and high values of electron-hole density are being created (as a result, e.g., of optical excitation by a pump laser or electrical current injection) and the subsequent probe by an appropriate optical ultrashort pulse.

*Electronic address: Ortwin.Hess@DLR.de

 

In this paper we self-consistently analyze on the basis of numerical simulations the microscopic nonequilibrium spatiotemporal dynamics of the interaction of transversely structured counterpropagating optical fields with the active semiconductor medium. Specifically, we discuss the excitation of a broad-area semiconductor laser by resonant and nonresonant continuous-wave (cw) Gaussian-shaped optical beams. In the simulation, the characteristic (counter) propagation of the optical fields within the active semiconductor layer is taken into account together with the transverse dynamics governed by diffraction as well as spatiotemporal carrier and temperature induced refractive index variations. This is done in combination with an appropriate representation of the spatially confined carrier injection, including the pump-blocking and injection heating effects [15], dynamic local carrier generation, carrier recombination by stimulated emission, as well as spatiotemporal changes in the energy distributions. As we will show, the complex interaction of these effects leads to dynamic variations in the local temperatures of the electron-hole plasma, the lattice, and, in particular, to characteristic nonequilibrium spatiospectral carrier and polarization Wigner distributions.

We will proceed along the following line. In Sec. II we extend our previous theory [2,4] on broad-area semiconductor lasers by including in the theory the combined optical and thermal spatiotemporal properties of the active laser medium. To model the spatiotemporal temperature dynamics we build on a moment expansion of the Boltzmann equation [16] and recent spatially homogeneous models of thermal effects in semiconductor lasers [17,18]. Specifically, the temperature elevation and relaxation is described on the basis of a balance-equation approach [19], where characteristic distributions of the phonon relaxation rates are taken into account. In Sec. III we discuss the spatiotemporal dynamics of the optical intensity distribution, the charge carrier density, refractive index, as well as the temperature of the lattice and the electron-hole plasma within the active zone of the broad-area laser. Section IV then presents our analysis of the nonequilibrium spatiospectral dynamics of the carrier Wigner distributions, where resonant as well as nonresonant excitation is discussed. Section V concludes the article.

## II. THEORETICAL DESCRIPTION

In the following, a theory for the description of the nonequilibrium spatiotemporal dynamics of spatially inhomogeneous semiconductor lasers is developed in which microscopic and macroscopic processes within the semiconductor layer are considered in combination with relevant thermal interactions. We emphasize that the general formulation of our theory allows, with consideration of the relevant microscopic material properties, description of many types of semiconductor lasers. For specificity, we will later concentrate on typical III-V semiconductor material systems, and use the relevant parameters for the GaAs-AlGaAs system [20].

### A. Semiconductor laser Maxwell-Bloch equations

Our theoretical description of nonequilibrium spatiotemporal dynamics of semiconductor lasers is based on a semiclassical approach. The optical fields are described by Maxwell's wave equation and the microscopic dynamics of the carrier distribution functions and interband polarization is governed by the semiconductor Bloch equations as derived in [4]. The microscopic system of equations is based on a Wigner function representation of the single particle density matrices [4] and thus generally holds for arbitrary spatially inhomogeneous geometries, such as multistripe laser, broad-area, and tapered edge emitting semiconductor lasers or coupled arrays of vertical cavity surface emitting lasers. In particular, spatial transport and momentum space dynamics have been self-consistently described using momentum and density dependent relaxation rates for the carrier distributions as well as for the polarization. The relaxation rate distributions include carrier-carrier scattering and carrier-phonon interactions. On the basis of this model we include in our present model on the microscopic and macroscopic levels the influence of spatiotemporally varying temperature distributions.

In the active zone of the semiconductor laser, the dynamics of the distribution of electrons ($e$) and holes ($h$) $f^{e,h}(k,\mathbf{r},t)$ and the interband polarizations $p_{\mathrm{nl}}^{\pm}(k,\mathbf{r},t)$ is governed by the equations of motion [4]

$$\frac{\partial}{\partial t}f^{e,h}(k,\mathbf{r},t)=g(k,\mathbf{r},t)-\tau_{e,h}^{-1}(k,N)[f^{e,h}(k,\mathbf{r},t)-f_{\mathrm{eq}}^{e,h}(k,\mathbf{r},t)]+\Lambda^{e,h}(k,\mathbf{r},t)-\Gamma_{\mathrm{sp}}(k,T_l)f^{e}(k,\mathbf{r},t)f^{h}(k,\mathbf{r},t)-\gamma_{\mathrm{nr}}f^{e,h}(k,\mathbf{r},t), \tag{1a}$$

$$\frac{\partial}{\partial t}p_{\mathrm{nl}}^{\pm}(k,\mathbf{r},t)=-[i\overline{\omega(}k,T_l)+\tau_p^{-1}(k,N)]p_{\mathrm{nl}}^{\pm}(k,\mathbf{r},t)+\frac{1}{i\hbar}d_{cv}(k)E^{\pm}(\mathbf{r},t)[f^{e}(k,\mathbf{r},t)+f^{h}(k,\mathbf{r},t)], \tag{1b}$$

with $k$ denoting the carrier-momentum wave number and $\mathbf{r}=(x,z)$, where $x$ and $z$ represent the lateral and longitudinal direction. $f_{\mathrm{eq}}^{e,h}(k,\mathbf{r},t)$ are the carrier distributions in thermal equilibrium with the lattice each given by the corresponding Fermi distribution. The counterpropagating optical fields $E^{\pm}(\mathbf{r},t)$ are governed by Maxwell's wave equations

$$\pm\frac{\partial}{\partial z}E^{\pm}(\mathbf{r},t)+\frac{n_l}{c}\frac{\partial}{\partial t}E^{\pm}(\mathbf{r},t)=\frac{i}{2}\frac{1}{K_z}\frac{\partial^2}{\partial x^2}E^{\pm}(\mathbf{r},t)-\left(\frac{\alpha(T_l)}{2}+i\eta\right)E^{\pm}(\mathbf{r},t)+\frac{i}{2}\frac{\Gamma}{n_l^2\epsilon_0 L}P_{\mathrm{nl}}^{\pm}(\mathbf{r},t), \tag{2}$$

where the polarization of the active semiconductor medium

$$P_{\mathrm{nl}}^{\pm}(\mathbf{r},t)=V^{-1}\sum_{\mathbf{k}}d_{cv}(k)p_{\mathrm{nl}}^{\pm}(k,\mathbf{r},t) \tag{3}$$

is the source of the optical fields. Here, $V$ denotes the normalization volume of the crystal and $d_{cv}(k)$ is the optical dipole matrix element. The interband polarizations $p^{\pm}_{\mathrm{nl}}(k,\mathbf{r},t)$ represent microscopically determined nonlinear spatiotemporal variations of the gain and the induced refractive index changes. In Eq. (2), $K_z$ denotes the wave number of the propagating fields, $n_l$ is the refractive index of the active layer, and $L$ is the length of the structure. Via the band gap energy, the linear absorption coefficient $\alpha$ depends on the lattice temperature $T_l$. Transverse ($x$) and vertical ($y$) variations of the refractive index due to the waveguide structure are included in the parameter $\eta$ and the waveguiding properties are described by the confinement factor $\Gamma$. The microscopic scattering rates $\tau^{-1}_{e,h}(k,N)$ in Eq. (1a) and $\tau^{-1}_{p}(k,N)$ in Eq. (1b) are microscopically determined [4] and include carrier-carrier scattering mechanisms and the interaction of carriers with optical phonons (LO phonons). Both are calculated in dependence on wave number and carrier density. $\Gamma_{\mathrm{sp}}(k,T_l)$ is the spontaneous recombination coefficient and $\gamma_{\mathrm{nr}}$ represents the rate due to nonradiative recombination. The frequency detuning $\overline{\omega}(k,T_l)$ between the cavity frequency $\omega$ and the transition frequency $\omega_T$ is given by

$$\hbar\overline{\omega}(k,T_l)=\mathcal{E}_g(T_l)+\frac{\hbar^2k^2}{2m_r}+\delta\mathcal{E}(\mathbf{r},t,T_l)-\omega$$
$$=\omega_T-\omega. \tag{4}$$

The transition frequency $\omega_T$ in turn depends via the band gap energy of the semiconductor medium on the carrier density and the lattice temperature $T_l$. Note that all variables which depend on $T_l$ implicitly include a dependence on space. The microscopic generation rate reads

$$g(k,\mathbf{r},t)=-\frac{1}{4i\hbar}d_{cv}(k)[E^{+}(\mathbf{r},t)p^{+}_{\mathrm{nl}}{}^{*}(k,\mathbf{r},t)$$
$$+E^{-}(\mathbf{r},t)p^{-}_{\mathrm{nl}}{}^{*}(k,\mathbf{r},t)]$$
$$+\frac{1}{4i\hbar}d^{*}_{cv}(k)[E^{+}{}^{*}(\mathbf{r},t)p^{+}_{\mathrm{nl}}(k,\mathbf{r},t)$$
$$+E^{-}{}^{*}(\mathbf{r},t)p^{-}_{\mathrm{nl}}(k,\mathbf{r},t)]. \tag{5}$$

The variation of the band gap with carrier density is given by [21]

$$\delta\mathcal{E}(\mathbf{r},t,T_l)=\mathcal{E}_0\frac{-a[N(\mathbf{r},t)a_0^3\mathcal{E}_0^2]^{1/4}}{[N(\mathbf{r},t)a_0^3\mathcal{E}_0^2+b^2(k_bT_l)^2]^{1/4}}, \tag{6}$$

with the exciton binding energy $\mathcal{E}_0=m_re^4/(2\epsilon_0^2\hbar^2)$, the exciton Bohr radius $a_0=\hbar^2\epsilon/(e^2m_r)$, the lattice temperature $T_l$, Boltzmann's constant $k_b$, the effective mass $m_r$, and the numerical factors $a=4.64$ and $b=0.107$. The dependence on the lattice temperature can be expressed as [22]

$$\mathcal{E}_g(T_l)=\mathcal{E}_g(0)-v_1T_l^2/(T_l+v_2), \tag{7}$$

where $\mathcal{E}_g(0)$ ($=1.519$ eV for GaAs) is the band gap at $T_l=0$ K, and $v_1$, $v_2$ are two material parameters given by $v_1=5.405\times10^{-4}$ eV/K and $v_2=204$ K for GaAs, respectively. The microscopic pump term

$$\Lambda^{e,h}(k,\mathbf{r},t)=\Lambda(\mathbf{r},t)\frac{f^{e,h}_{\mathrm{eq}}(k,\mathbf{r},t)[1-f^{e,h}(k,\mathbf{r},t)]}{V^{-1}\sum_{\mathbf{k}}f^{e,h}_{\mathrm{eq}}(k,\mathbf{r},t)[1-f^{e,h}(k,\mathbf{r},t)]} \tag{8}$$

represents the pump-blocking effect. The macroscopic pump term

$$\Lambda(\mathbf{r},t)=\frac{\eta_{\mathrm{eff}}}{ed}\mathcal{J}(\mathbf{r},t) \tag{9}$$

includes the generally space dependent and time dependent injection current density $\mathcal{J}(\mathbf{r},t)$, where $\eta_{\mathrm{eff}}$ is the quantum efficiency and $d$ is the thickness of the active layer.

### B. Ambipolar transport and temperature dynamics

The microscopic semiconductor dynamics is generally described by the distribution functions of electrons and holes as well as by the interband polarization [cf. Eq. (1)]. Being Wigner distributions, they are functions of space and momentum. As has been discussed in [4], compared to the **k**-space relaxation of the microscopic variables towards their local quasiequilibrium values on a femtosecond time scale the spatial transport of charge carriers occurs on a much slower time scale in the picosecond up to the nanosecond regime (10 ps, . . . ,10 ns). This typical separation of time scales between the **k**-space and the **r**-space dynamics allows us to treat both regimes separately, with the influence of spatial gradients on the **k**-space dynamics often being negligible.

Retaining the first order spatial derivatives of the distribution functions and neglecting any spatial transport of polarization, the equations of motion for electron and hole distribution functions are given by two Boltzmann equations

$$\frac{\partial}{\partial t}f^{e,h}(k,\mathbf{r},t)+\frac{\hbar\mathbf{k}}{m_{e,h}}\cdot\frac{\partial f^{e,h}(k,\mathbf{r},t)}{\partial\mathbf{r}}-\frac{1}{\hbar}\left(\frac{\partial\delta\mathcal{E}(\mathbf{r},t)}{\partial\mathbf{r}}\right.$$
$$\left.\mp e\frac{\partial\phi(\mathbf{r})}{\partial\mathbf{r}}\right)\cdot\frac{\partial f^{e,h}(k,\mathbf{r},t)}{\partial\mathbf{k}}$$
$$=\left.\frac{\partial f^{e,h}(k,\mathbf{r},t)}{\partial t}\right|_{col}+g(\pm\mathbf{k},\mathbf{r},t)+\Lambda^{e,h}(k,\mathbf{r},t)$$
$$-\Gamma_{\mathrm{sp}}(k)f^{e}(\pm\mathbf{k},\mathbf{r},t)f^{h}(\mp\mathbf{k},\mathbf{r},t)-\gamma_{\mathrm{nr}}f^{e,h}(k,\mathbf{r},t), \tag{10}$$

where the upper (lower) sign refers to electrons (holes). The scattering term $\partial f^{e,h}/\partial t|_{col}$ generally may include carrier-carrier and carrier-phonon scattering processes, which in analogy to Eq. (1) we will later express in terms of suitable relaxation rates. Due to the charge of the carriers, the electron-hole plasma is additionally characterized by a Poisson equation

$$-\nabla\cdot\mathbf{\Phi}(\mathbf{r})=\nabla^2\phi(\mathbf{r})=-\frac{1}{\varepsilon_0}\rho(\mathbf{r})$$
$$=\frac{e}{\varepsilon_0}V^{-1}\sum_{\mathbf{k}}[f^{e}(k,\mathbf{r})-f^{h}(k,\mathbf{r})] \tag{11}$$

for the electric field $\mathbf{\Phi}(\mathbf{r})$, with the electrostatic potential $\phi(\mathbf{r})$. The space-charge density $\rho(\mathbf{r})$ is determined by the carrier-distribution functions.

Integration of the Boltzmann equations for the charge carrier distributions allows determination of a series of moments and corresponding equations of motion. In lowest order those are the charge carrier densities

$$N^{e,h}(\mathbf{r},t)=V^{-1}\sum_{\mathbf{k}} f^{e,h}(k,\mathbf{r},t), \tag{12}$$

the current densities (moments of first order)

$$\mathbf{j}^{e,h}(\mathbf{r},t)=V^{-1}\sum_{\mathbf{k}} \frac{\hbar\mathbf{k}}{m_{e,h}} f^{e,h}(k,\mathbf{r},t), \tag{13}$$

and the energy densities (moments of second order)

$$\begin{aligned} u^{e,h}(\mathbf{r},t)&=V^{-1}\sum_{\mathbf{k}} \frac{\hbar^2k^2}{2m_{e,h}} f^{e,h}(k,\mathbf{r},t)\\ &=V^{-1}\sum_{\mathbf{k}} \epsilon^{e,h}(k) f^{e,h}(k,\mathbf{r},t) \end{aligned} \tag{14}$$

of electrons ($e$) and holes ($h$). Notationally suppressing the space and time dependence, the resulting (hydrodynamic) equations of motion read

$$\frac{\partial}{\partial t}N^{e,h}+\nabla\cdot\mathbf{j}^{e,h}=\Lambda^{e,h}+G-\gamma_{\rm nr}N^{e,h}-W + V^{-1}\sum_{\mathbf{k}} \frac{\partial}{\partial t} f^{e,h}(k)|_{col}, \tag{15a}$$

$$\begin{aligned} &\frac{\partial}{\partial t}\mathbf{j}^{e,h}+\frac{1}{N^{e,h}}(\nabla\cdot\mathbf{j}^{e,h})\mathbf{j}^{e,h}+\frac{1}{N^{e,h}}(\mathbf{j}^{e,h}\cdot\nabla)\mathbf{j}^{e,h}\\ &\quad+\nabla\cdot(N^{e,h}k_B\mathcal{T}^{e,h})-\frac{N^{e,h}}{\hbar}(\nabla\delta\mathcal{E}\mp e\nabla\phi)\\ &=\Lambda_j^{e,h}+G_j-\gamma_{\rm nr}\mathbf{j}^{e,h}-W_j\\ &\quad+V^{-1}\sum_{\mathbf{k}} \frac{\hbar\mathbf{k}}{m_{e,h}}\frac{\partial}{\partial t} f^{e,h}(k)|_{col}, \end{aligned} \tag{15b}$$

$$\begin{aligned} &\frac{\partial}{\partial t}u^{e,h}+\nabla\cdot(\mathbf{j}^{e,h}u^{e,h})+\nabla\cdot(k_B\mathcal{T}^{e,h}\cdot\mathbf{j}^{e,h})+\nabla\cdot\mathbf{Q}^{e,h}\\ &-\frac{\mathbf{j}^{e,h}}{\hbar}\cdot(\nabla\delta\mathcal{E}\mp e\nabla\phi)\\ &=+\Lambda_u^{e,h}+G_u^{e,h}-\gamma_{\rm nr}u^{e,h}-W_u^{e,h}\\ &\quad+V^{-1}\sum_{\mathbf{k}} \frac{\hbar^2\mathbf{k}^2}{2m_{e,h}}\frac{\partial}{\partial t} f^{e,h}(k)|_{col}. \end{aligned} \tag{15c}$$

The heat flux $\mathbf{Q}^{e,h}$ and the temperature tensor $\mathcal{T}_{\mu\nu}^{e,h}$ are represented by

$$\mathbf{Q}^{e,h}=-\kappa\nabla T^{e,h}, \tag{16}$$

$$\mathcal{T}_{\mu\nu}^{e,h}=T^{e,h}\delta_{\mu\nu}, \tag{17}$$

where $\kappa$ is a phenomenological heat conductivity and $\delta_{\mu\nu}$ the Kronecker-delta symbol. Adopting the relaxation-rate approximation of the scattering terms as described in [4], the current density is expressed as

$$\mathbf{j}^{e,h}=-D^{e,h}\nabla N^{e,h}\pm\sigma^{e,h}\frac{1}{e}\nabla\phi, \tag{18}$$

with the diffusivities

$$D^{e,h}=-\frac{1}{3}V^{-1}\sum_{\mathbf{k}} \tau_{e,h}(k,N)\frac{\hbar^2k^2}{m_{e,h}^2}\frac{\partial f_{\rm eq}^{e,h}(k)}{\partial\epsilon^{e,h}(k)}\frac{\partial(\tilde{\mu}^{e,h}+\delta\mathcal{E})}{\partial N^{e,h}} \tag{19}$$

and the conductivities

$$\sigma^{e,h}=N^{e,h}e\tilde{\mu}^{e,h}=-\frac{e^2}{3}V^{-1}\sum_{\mathbf{k}} \tau_{e,h}(k,N)\frac{\hbar^2k^2}{m_{e,h}^2}\frac{\partial f_{\rm eq}^{e,h}(k)}{\partial\epsilon^{e,h}(k)}, \tag{20}$$

where $\tilde{\mu}^{e,h}$ denote electron and hole mobilities.

The spatial transport of electrons and holes is coupled by electrostatic forces expressed by the electrostatic potential $\phi$ which, in turn, is obtained from the carrier densities by solving Poisson's equation (11). The coupling strongly increases with increasing carrier densities. This eventually results in ambipolar transport of electrons and holes [4]. Then, no space charges exist and the densities of electrons and holes are equal, $N^e=N^h=N$ . In order to keep this neutrality, also the current densities are equal, $\mathbf{j}^e=\mathbf{j}^h=\mathbf{j}$. Eliminating the drift term in Eq. (18) results in the ambipolar diffusion current density

$$\mathbf{j}=-D_f\nabla N, \tag{21}$$

with the ambipolar diffusion coefficient

$$D_f=\frac{\sigma^hD^e+\sigma^eD^h}{\sigma^e+\sigma^h}\ . \tag{22}$$

Under nondegenerate conditions, where due to the Einstein relation $\sigma^e/\sigma^h=D^e/D^h$ holds, Eq. (22) reduces to the well-known form $D_f^{-1}=\frac{1}{2}(D^{e-1}+D^{h-1})$ [23,16,24]. Combining Eqs. (15a) and (21), and approximating the space dependence of the energy densities with a parametric representation, the macroscopic transport equation for the carrier density $N(\mathbf{r},t)$ and the relaxation equation for the energy densities $u^{e,h}(\mathbf{r},t)$ are given by

$$\frac{\partial}{\partial t}N(\mathbf{r},t)=\nabla\cdot[D_f\nabla N(\mathbf{r},t)]+\Lambda(\mathbf{r},t)+G(\mathbf{r},t)-\gamma_{\rm nr}N(\mathbf{r},t) - W(\mathbf{r},t), \tag{23a}$$

$$\frac{\partial}{\partial t}u^{e,h}(\mathbf{r},t)=\Lambda_u^{e,h}(\mathbf{r},t)+G_u^{e,h}(\mathbf{r},t)-\gamma_{\rm nr}u^{e,h}(\mathbf{r},t)-W_u^{e,h}(\mathbf{r},t) - R^{e,h}(\mathbf{r},t). \tag{23b}$$

In Eq. (23) we have considered spatially structured carrier injection ($\Lambda$ and $\Lambda_u^{e,h}$), carrier recombination by stimulated emission ($G$ and $G_u^{e,h}$), nonradiative recombination ($\gamma_{\rm nr}N$ and $\gamma_{\rm nr}u^{e,h}$), and spontaneous emission ($W$ and $W_u^{e,h}$). Note that due to the parametric representation of the energy transport processes adopted here, the phonon relaxation term $R^{e,h}$ (detailed below) appears directly in Eq. (23b) for the energy densities, whereas the microscopic carrier-phonon and carrier-carrier interactions enter indirectly into the ambipolar diffusion equation (23a) via $D_f$. The macroscopic gain

$$G(\mathbf{r},t)=\frac{\chi''\epsilon_0}{2\hbar}[|E^+(\mathbf{r},t)|^2+|E^-(\mathbf{r},t)|^2] - \frac{1}{4\hbar}\mathrm{Im}[E^+(\mathbf{r},t)P_{\rm nl}^{+}{}^*(\mathbf{r},t) + E^-(\mathbf{r},t)P_{\rm nl}^{-}{}^*(\mathbf{r},t)] \tag{24}$$

with Im[z] denoting the imaginary part of $z$, describes the spatiotemporal variation of both the induced emission and the absorption of light. It depends via the polarizations (3) on the microscopic charge carrier distribution functions, which, in turn, both depend on the plasma temperatures $T_{\rm pl}^{e,h}$ of electrons and holes, respectively. The frequency $\overline{\omega}$ depends via the band gap energy (4) on the lattice temperature. The spontaneous emission is related to the microscopic carrier Wigner distributions $f^{e,h}$ by

$$W(\mathbf{r},t)=\frac{1}{V}\sum_{\mathbf{k}}\ \Gamma_{\rm sp}(k,T_l)f^e(k,\mathbf{r},t)f^h(k,\mathbf{r},t), \tag{25}$$

with the phenomenological rate of spontaneous emission [25]

$$\Gamma_{\rm sp}(k,T_l)=\frac{n_l}{\epsilon_0\hbar\pi}|d_{cv}(k)|^2\left(\mathcal{E}_g(T_l)+\frac{\hbar^2k^2}{2m_r}\right)^3. \tag{26}$$

It generally depends on the temperatures of the electron and hole plasma $T^{e,h}$ as well as on the lattice temperature $T_l$. In the relaxation equation (23b) for the energy densities the corresponding rates are given by

$$\Lambda_u^{e,h}(\mathbf{r},t)=\frac{1}{V}\sum_{\mathbf{k}}\ \epsilon^{e,h}(k)\Lambda^{e,h}(k,\mathbf{r},t), \tag{27a}$$

$$G_u^{e,h}(\mathbf{r},t)=-\frac{1}{2\hbar^2V}[|E^+(\mathbf{r},t)|^2+|E^-(\mathbf{r},t)|^2] \times\frac{1}{V}\sum_{\mathbf{k}}\ \epsilon^{e,h}(k)\frac{\tau_p^{-1}(k,N)}{\overline{\omega^2}(k,T_l)+\tau_p^{-2}(k,N)} \times|d_{cv}(k)|^2[f^e(k,\mathbf{r},t)+f^h(k,\mathbf{r},t)-1], \tag{27b}$$

$$W_u^{e,h}(\mathbf{r},t)=\frac{1}{V}\sum_{\mathbf{k}}\ \epsilon^{e,h}(k)\Gamma_{\rm sp}(k,T_l)f^e(k,\mathbf{r},t)f^h(k,\mathbf{r},t). \tag{27c}$$

The relaxation term

$$R^{e,h}(\mathbf{r},t)=\sum_{\rm ph}\ \frac{1}{\tau_{\rm ph}^{e,h}}[u^{e,h}(\mathbf{r},t)-u_{\rm eq}^{e,h}(\mathbf{r},t)] +\frac{1}{V}\sum_{\mathbf{k}}\ \frac{\hbar^2k^2}{2m_{e,h}}\frac{1}{\tau_{\rm PO}^{e,h}(k,N)}[f^{e,h}(k,\mathbf{r},t) -f_{\rm eq}^{e,h}(k,\mathbf{r},t)] \tag{28}$$

describes the change in energy due to carrier-phonon interactions. The phonons involved include polar optical phonons (LO phonons), deformation potential optical phonons (only holes), deformation potential acoustic phonons, and carrier-piezoelectric acoustic phonons. The polar optical phonons are again calculated according to the carrier density for each value of the wave number whereas the other contributions are considered as averaged values which we adopt from the detailed phonon rate calculations in [18]. The first term in Eq. (28) represents via their respective relaxation rates abbreviated by $1/\tau_{\rm ph}^{e,h}$ the sum over all the phonon contributions except for the polar optical phonon scattering rates. For consistency, the latter are considered via the microscopic momentum and density dependent scattering rates $1/\tau_{\rm po}^{e,h}(k,N)$ (for their dependence of $N$ and $k$, see [4], Fig. 1). An extension to a carrier and wave number dependent consideration of all phonon rates will be straightforward. We note that due to the Poisson equation directly acting only on the charge carrier density and the momentum density, differentiation between the different energy densities of electrons and holes has to be made due to their difference in relaxation times and effective masses.

On the basis of a grand canonical ensemble interpretation having both energy and particle contact and exchange with the environment, we consider the carrier density and the carrier energies as functions of the independent variables of the chemical potentials $\mu^{e,h}$ and the plasma temperatures $T_{\rm pl}^{e,h}$. Solving the resulting set of equations for the plasma temperatures $T_{\rm pl}^{e,h}$ leads to

$$\dot{T}_{\rm pl}^{e,h}(\mathbf{r},t)=J_u^{e,h}(\mathbf{r},t)\frac{\partial u^{e,h}(\mathbf{r},t)}{\partial t}-J_N^{e,h}(\mathbf{r},t)\frac{\partial N(\mathbf{r},t)}{\partial t}, \tag{29}$$

where $J_u$ and $J_N$ are given by

$$J_u^{e,h}(\mathbf{r},t)=\frac{\partial N^{e,h}}{\partial\mu^{e,h}}\left(\frac{\partial u^{e,h}(\mathbf{r},t)}{\partial T_{\rm pl}^{e,h}(\mathbf{r},t)}\frac{\partial N^{e,h}(\mathbf{r},t)}{\partial\mu^{e,h}(\mathbf{r},t)} -\frac{\partial u^{e,h}(\mathbf{r},t)}{\partial\mu^{e,h}(\mathbf{r},t)}\frac{\partial N^{e,h}(\mathbf{r},t)}{\partial T_{\rm pl}^{e,h}(\mathbf{r},t)}\right)^{-1}, \tag{30}$$

$$J_N^{e,h}(\mathbf{r},t)=\frac{\partial u^{e,h}}{\partial\mu^{e,h}}\left(\frac{\partial u^{e,h}(\mathbf{r},t)}{\partial T_{\rm pl}^{e,h}(\mathbf{r},t)}\frac{\partial N^{e,h}(\mathbf{r},t)}{\partial\mu^{e,h}(\mathbf{r},t)} -\frac{\partial u^{e,h}(\mathbf{r},t)}{\partial\mu^{e,h}(\mathbf{r},t)}\frac{\partial N^{e,h}(\mathbf{r},t)}{\partial T_{\rm pl}^{e,h}(\mathbf{r},t)}\right)^{-1}. \tag{31}$$

The multitude of processes determining the lattice temperature are the relaxation to the ambient temperature $T_a$ (relax-

TABLE I. Fundamental material and device parameters of the broad-area (GaAs/AlGaAs) semiconductor lasers.

| | |
|---|---|
| $L$ (cavity length) | 750 $\mu$m |
| $d$ (thickness of active layer) | 0.15 $\mu$m |
| $n_c$ [refractive index of the cladding layers (GaAlAs)] | 3.35 |
| $n_l$ [refractive index of active layer (GaAs)] | 3.59 |
| $\lambda$ (laser wavelength) | 815 nm |
| $R_1$ (front facet mirror reflectivity) | $10^{-4}$ |
| $R_2$ (back facet mirror reflectivity) | $10^{-4}$ |
| $\tau_{\rm nr}$ (nonradiative recombination time) | 5 ns |
| $a_0$ (exciton Bohr radius) | $1.243\times10^{-6}$ cm |
| $m_0$ (mass of the electron) | $9.1093879\times10^{-31}$ kg |
| $m_e$ (effective electron mass) | $0.067m_0$ |
| $m_h$ (effective hole mass) | $0.246m_0$ |
| $\mathcal{E}_g(0)$ (semiconductor energy gap at $T=0$ K) | 1.519 eV |
| $D_p$ (diffraction coefficient) | $18\times10^{-6}m$ |
| $\eta_i$ (injection efficiency) | 0.5 |
| $\Gamma$ (confinement factor) | 0.55/0.54 |
| $\alpha_w$ (absorption) | 30 cm$^{-1}$ |
| $v_{\rm sr}$ (surface recombination velocity) | $10^6$ m/s |

ation constant $-\gamma_a$), the transfer of heat from the plasma to the lattice due to carrier-phonon scattering (again considered microscopically for the case of the LO phonons), nonradiative recombination (where $c_q$ is the specific heat) and Joule heating (with total resistance $R$, cross section $A$, and volume of the active zone of the broad-area laser $V_{\rm BAL}$) leading to

$$\begin{aligned}\dot{T}_l(\mathbf{r},t)=&-\gamma_a[T_l(\mathbf{r},t)-T_a]+\sum_{\rm ph}\frac{1}{\tau^e_{\rm ph}}[T^e_{\rm pl}(\mathbf{r},t)-T_l(\mathbf{r},t)]\\&+J^e_u(\mathbf{r},t)\frac{1}{\pi^2}\frac{1}{V}\sum_{\mathbf{k}}\frac{\hbar^2k^2}{2m_e}\frac{1}{\tau^e_{\rm PO}}[f^e(k,\mathbf{r},t)\\&-f^e_{\rm eq}(k,\mathbf{r},t)]+\sum_{\rm ph}\frac{1}{\tau^h_{\rm ph}}[T^h_{\rm pl}[\mathbf{r},t)-T_l(\mathbf{r},t)]\\&+J^h_u(\mathbf{r},t)\frac{1}{\pi^2}\frac{1}{V}\sum_{k}\frac{\hbar^2k^2}{2m_h}\frac{1}{\tau^h_{\rm PO}}[f^h(k,\mathbf{r},t)\\&-f^h_{\rm eq}(k,\mathbf{r},t)]+\hbar\omega\gamma_{\rm nr}N(\mathbf{r},t)+\frac{\mathcal{J}^2(r,t)RA^2}{c_qV_{\rm BAL}}.\end{aligned}\tag{32}$$

For the numerical integration of the system of partial differential equations (2) and (23a) the *Hopscotch* method [26] is used as a general scheme. At every spatial location it is self-consistently coupled and solved with the microscopic equations for the carrier and polarization Wigner distributions (1) and the temperature equations of the lattice (32) and the plasma (29). The operators are discretized by the *Lax-Wendroff* [27] method. The material and structural parameters are summarized in Table I.

## III. SPATIOTEMPORAL DYNAMICS

The coupled system of microscopic and macroscopic equations for the semiconductor laser are the basis for the numerical simulations presented and discussed below. Specifically, we consider the broad-area semiconductor laser geometry, schematically depicted in Fig. 1. An active semiconductor layer (here: GaAs) into which current is injected through a characteristically wide current stripe is sandwiched between cladding layers (here $Al_xGa_{1-x}As$). Broad-area lasers are usually realized as gain-guided structures, i.e., the optical waveguiding properties necessary for channeling the optical fields along the longitudinal direction are self-generated by differences in local gain. We model the spatiotemporal dynamics of a typical broad-area laser. The transverse width $w=100$ $\mu$m and its longitudinal length $L=750$ $\mu$m are typical values of commercially available devices. In the simulations, the laser is electrically pumped at a few times its threshold current. A continuous-wave Gaussian-shaped optical beam is injected from the left and is amplified while propagating to the right. Its spatially inte-

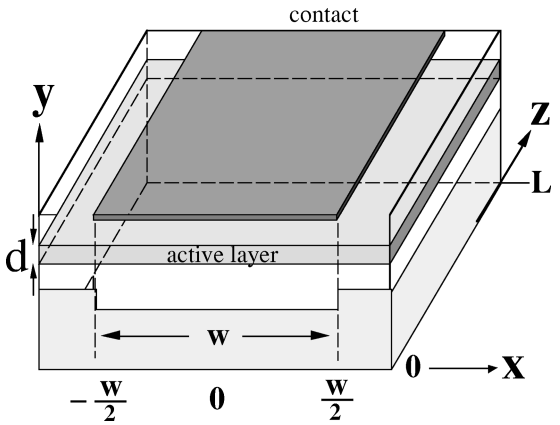


FIG. 1. Schematic of the geometry of a broad-area semiconductor laser. Charge carriers injected through the contact stripe at the top of the device (hatched) recombine in the active zone. The active GaAs layer (shaded dark) is located between two cladding layers of $Al_xGa_{1-x}As$ (white). Light generated by stimulated emission and amplification propagates in longitudinal ($z$) direction.

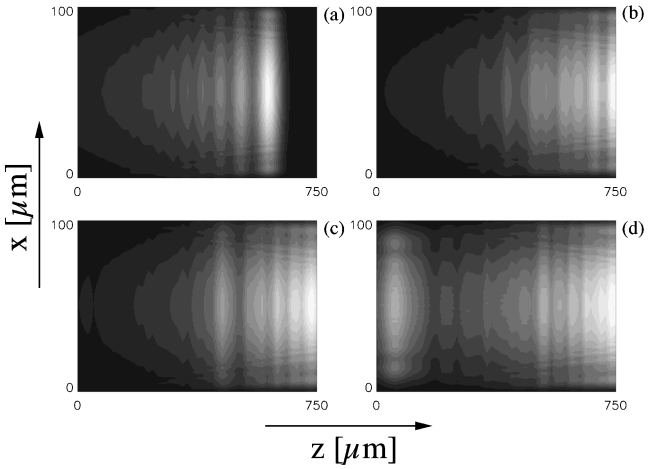


FIG. 2. Amplification and longitudinal self-structuring of an injected optical cw signal within the active layer of a broad-area semiconductor laser. The individual plots display snapshots of the intracavity intensity $I(x,z,t_0)\sim[|E^+(x,z,t_0)|^2+|E^-(x,z,t_0)|^2]$, taken at intervals of 10 ps with the area in each individual plot corresponding to the full active zone of the laser. The power of the injected optical cw signal is $P_{\mathrm{inj}}=10$ mW. Dark shading corresponds to low intensity and bright colors to areas of high intensity. The optical signal is injected from the left and the outcoupling facet is located at the right side of the laser. Its transverse stripe width is $w=100$ $\mu$m. The longitudinal extension corresponds to 750 $\mu$m.

grated power is 10 mW at the input facet.

As a result of its characteristic geometry, the broad-area structure constitutes a model system of a one-transverse-dimensional system showing spontaneous formation and dynamics of nonlinear optical patterns and gratings [5]. But it is not only in the transverse $x$ dimension where spontaneous self-structuring occurs. Once its longitudinal resonator length exceeds a characteristic internal (coherence) length, the optical field may additionally display dynamic structuring in longitudinal direction during propagation. Figure 2 displays a number of snapshots of the intensity distribution in the quasi-two-dimensional active zone of the broad-area laser. The time difference between successive plots is 10 ps. Figure 2(a) shows the intensity $I(x,z)\sim|E^+(x,z)|^2+|E^-(x,z)|^2$ at 10 ps after starting injection of the optical beam. At this time, the incoming beam has not yet reached the output facet. During propagation, the optical field continuously interacts with the active semiconductor medium. As a consequence combined self-focusing and diffraction effects lead to the observed longitudinal modulation and transverse structuring in the intensity distribution. This self-structuring is characteristic for the high-gain semiconductor laser structures and occurs although the pump profile due to carrier injection and shape of the input beam are assumed to be uniform. The origin of these phenomena is related to the internal microscopic carrier-carrier and carrier-phonon scattering processes and charge carrier transport. Both lead to a characteristic fast momentum relaxation of the carriers and dephasing of the polarization on a time scale on the order of $\approx$50–100 fs [4]. Together with typical propagation times $\sim$10 ps this corresponds to an internal longitudinal coherence length $\ell$ of about 50 to 100 $\mu$m. The typical diffusion length of the charge carriers is in the order of 5 to 10 $\mu$m. With the longitudinal length $L=750$ $\mu$m of our laser being considerably larger than $\ell$, longitudinal self-structuring sets in and, in combination with the transverse self-focusing effects, about ten intensity peaks with irregular periodicity are formed.

Once the incoming beam has reached the outcoupling facet at the right (reflectivity $R_2=10^{-4}$) part of the field is reflected [Fig. 2(b)]. As a consequence, the self-structuring effects appear even stronger due to the additional interaction of the continuously incoming and forward propagating beam with the reflected backward propagating field. In spite of the extremely low reflectivities $\sim10^{-4}$ used in the calculation, the high gain within the active semiconductor layer effectively creates a much higher facet reflectivity. Indeed, the counterpropagation effects are always present in semiconductor lasers and amplifiers with large active areas—even when assuming ''perfect'' antireflecting coatings with $R_1=R_2=0$. This can be understood by the formation of a dynamic diffraction grating in the carrier density. As a consequence of the difference in time scales of optical diffraction and carrier diffusion, the intensity in the laser continuously varies in time and space—even after the injected signal has reached the output facet. The intensity at the output facet thus fluctuates in its amplitude and a fraction of the light in the laser is traveling backward and forward in the resonator. This can be observed in the time series of Fig. 2. Note that due to diffraction of the optical fields, part of the reflected light also propagates at an off angle with respect to the main propagation direction towards the absorbing layers. For longer times with more round-trips, the spatiotemporal variations in the intensity distribution continue to become increasingly complex within the whole active zone of the laser [5]. In the following, however, we will continue to concentrate our analysis on the early stages of the buildup of the spatiotemporal instabilities. Specifically we will consider a characteristic scenario where an optical beam is injected into the broad-area semiconductor laser. From the spatiotemporal dynamics we will pick characteristic instants in time (about 20 ps after the beginning of the optical injection) and discuss the various distributions of optical and material properties of the active semiconductor medium.

The perpetual interaction of the optical field with the active semiconductor medium is most clearly highlighted in the characteristic distributions of the charge carrier density, the gain, and the refractive index. The snapshots in Fig. 3 show the characteristic structural differences in the spatial variation of the intensity, the density, the macroscopic gain, and the refractive index at one instant in time. As expected, the amplification of the injected radiation leads to a local reduction in the density distribution and thus to depletion of the gain. Note that in Eq. (24) $G$ is defined as generation rate (i.e., ''negative gain''); consequently Fig. 3 shows its inverse. Due to the differences in the characteristic time scales of the polarization and density (intercavity lifetime of a photon: 1–10 ps; momentum relaxation of the carriers: $\approx$50 fs), the inversion is not instantaneously transformed into light. Consequently, the density has a spatial and temporal offset to the inverse of the intensity distribution. The snapshot of the gain shown in Fig. 3(c) thus reflects the spatial structure of both the carrier density and the intensity [see Eq. (24)]. It simultaneously exhibits the small modulations of the inten-

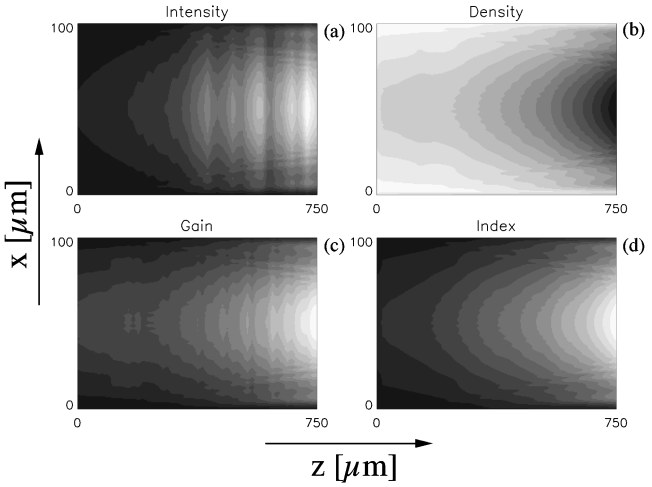


FIG. 3. Snapshot images of the intensity $I(x,z,t_0)$, charge carrier density $N(x,z,t_0)$, gain $G(x,z,t_0)$, and nonlinear (induced) refractive index distribution $\delta n(x,z,t_0)/n(x,z,t_0)=\chi'/2$ in the active layer of the broad-area laser. The power of the injected cw signal is $P_{\mathrm{inj}}=10$ mW.

sity distribution and the spatial distribution of the density. From Fig. 3(d) we see that the refractive index is increased with respect to the basic linear refractive index at positions of high intensity and low density. This leads to self-focusing which again affects the optical properties of the light field in the instant thereafter. Generally, all distributions displayed in Fig. 3 are affected by the nonvanishing reflectivities of the facets. They have as a consequence not only the characteristic transverse filamentlike optical patterns in the intensity distribution, but also spatial structuring in the other variables. The influence is particularly strong in those areas of the active layer which are not as strongly influenced by the incoming beam such as the center of the laser. An analysis of the distribution of the refractive index provides a good possibility for visualizing the filament formation: For high injection currents and poorly coated structures, the distributions in the device are much more influenced by the internal spatiotemporal dynamics and the geometry of the semiconductor laser itself than by the characteristics of the input beam. In this case irregular patterns are formed in the refractive index over the whole transverse width. These transverse variations then are the origin for the characteristic formation of optical filaments in wide-gain amplifiers and lasers.

Next to direct dependence of the refractive index on the local distribution of carriers, the optical generation of heat and its relaxation via phonons to the temperature of the lattice significantly determine the optical properties and the spatiotemporal dynamics of the broad-area laser. Figure 4 shows in direct comparison to the intensity snapshot images of the temperature distributions of the lattice [Fig. 4(b)], the electrons [Fig. 4(c)], and the holes [Fig. 4(d)]. Generally, high local intensity values cause a strong interchange between carriers and phonons. At this position, this leads to an increase in the temperature of the lattice. The stimulated recombination of the carriers, however, occurs at energy values below the average energy; the carrier ensemble thus obtains an increased average energy. As a result, the temperature of the electron-hole plasma is locally increased in the areas with high optical intensity and a strong negative gain (i.e., absorption). We note that due to the differences in their effective mass and phonon relaxation rates, the spatial distribution of the electron plasma deviates from the hole plasma.

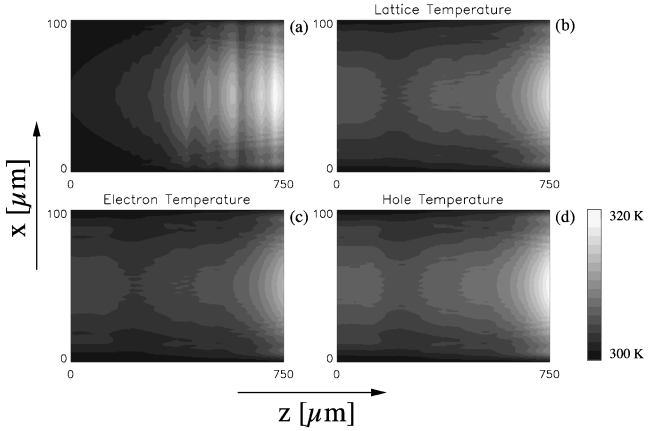


FIG. 4. Same time instant as in Fig. 3. Images of the spatial temperature distribution of the lattice temperature, the electron and hole temperature in comparison with the corresponding intensity distribution show the spatial differences between the distributions.

## IV. NONEQUILIBRIUM WIGNER DISTRIBUTIONS

In the simulation, the dynamics of the microscopic properties—which determine the macroscopic variables discussed so far—are self-consistently determined at every spatial location. Before we discuss the Wigner distribution, which includes both the spatial and spectral dependence of the carrier distributions and the interband polarization functions, we will briefly illustrate characteristic spectral properties of semiconductor lasers—dependence of the generation rate and the nonlinear induced refractive index on the wavelength of light.

### A. Equilibrium gain spectrum and refractive index dispersion

The spectral characteristics of the active semiconductor medium during propagation and amplification of an optical input beam are contained in the microscopic carrier distributions, polarizations, and generation rates. As an example, Fig. 5 shows the spectral dependence of the spatially averaged generation rate $g(k,t)$ [cf. Eq. (1a)] for various values of the electron-hole density. Via $\overline{\omega}$, the generation rate $g$ is determined indirectly by the lattice and plasma temperatures and directly via the carrier distributions. Figure 5 shows that with increasing injection current and increased carrier density the generation rate changes from absorption to amplification and increases in magnitude. The microscopic complex optical susceptibility

$$\chi(\omega)=\chi'(\omega)+i\chi''(\omega) \tag{33a}$$

$$=-\frac{1}{\hbar V}\sum_{k}|d_{cv}(k)|^2\frac{[f^e(k,\mathbf{r},t)+f^h(k,\mathbf{r},t)-1]}{\overline{\omega}(k,T_l)-i\tau_p^{-1}(k,N)} \tag{33b}$$

locally depends on the frequency $\omega$, the lattice temperature $T_l$ via $\overline{\omega}$, the plasma temperatures $T_{\mathrm{pl}}^{e,h}$ via $f^{e,h}$, and the

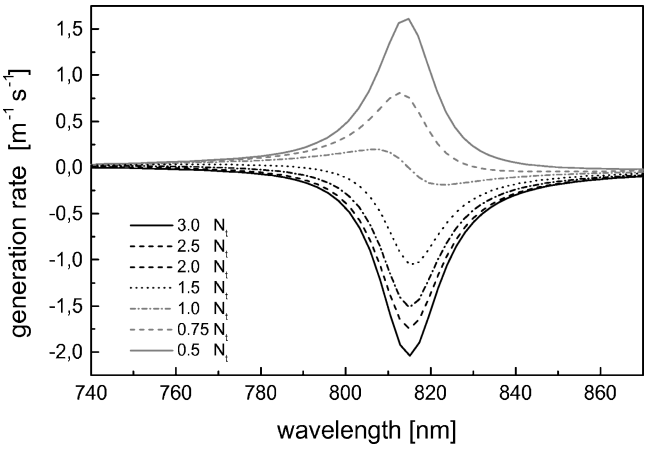


FIG. 5. From absorption to stimulated recombination. The wavelength dependence of the generation rate $g$ for various values of the charge carrier density in the broad-area laser shows for increasing carrier density the transition from net absorption ($N<N_t$) to net gain ($N>N_t$), with $N_t$ being the transparency density.

charge carrier density $N$. It gives information on both the generation rate via Eq. (1a) and through [28]

$$\frac{\delta n}{n_l}=\frac{\chi'}{2} \tag{34}$$

on the induced refractive index $\delta n/n_l$. For fixed lattice temperature $T_l=300$ K its wavelength dependence is displayed in Fig. 6 for various values of the carrier density. In particular, when raising $N$ above the transparency density $N_t$, the wavelength dependence of $\delta n/n_l$ displays the characteristic change in sign and shows the expected dispersion. Note that in Eq. (34) the whole nonlinearity is included and not only the first or second order term of an expansion in $E$.

### B. Nonequilibrium spatiospectral distributions

As shown in Fig. 5, with increasing carrier density a transition from absorption to stimulated emission occurs. In the case of our model semiconductor laser, due to its considerable resonator length ($L=750$ $\mu$m), many longitudinal optical modes potentially lie within the spectral width of the

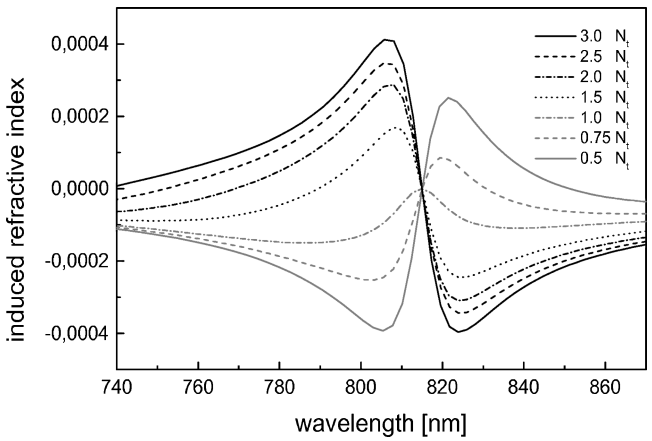


FIG. 6. Influence of increasing electron-hole density $N$ (in units of the transparency density $N_t$) on the dispersion of the induced nonlinear refractive index $\delta n/n_l$.

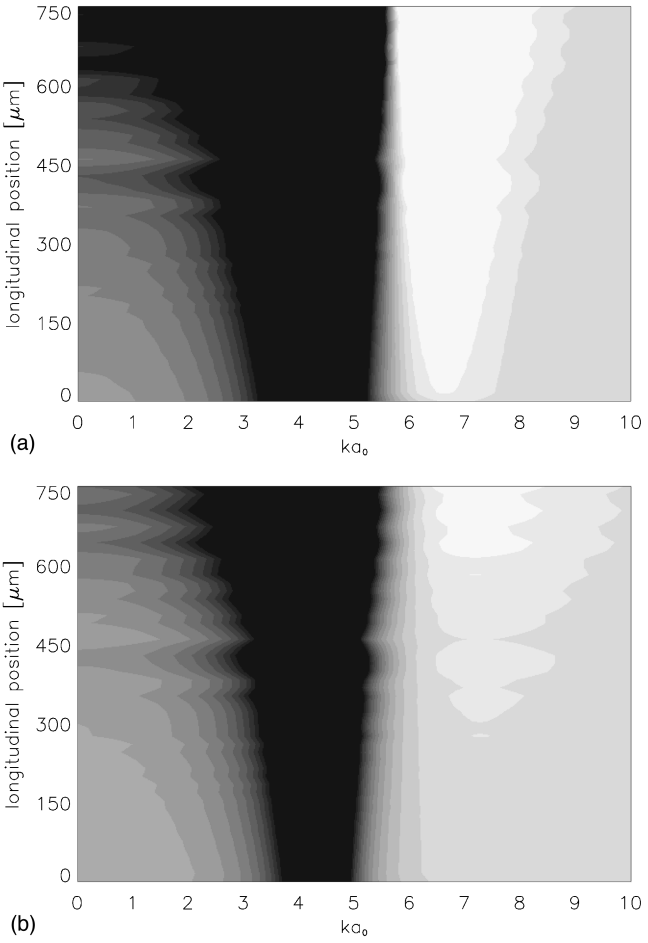


FIG. 7. Snapshots of the nonequilibrium carrier Wigner distributions. In the gray-scale plots of the longitudinal space and momentum dependence of (a) the electron Wigner distribution $\delta f_z^e(k,z,t_0)$ and (b) the hole Wigner distribution $\delta f_z^h(k,z,t_0)$ medium gray areas represent $\delta f_z^e(k,z,t_0)=\delta f_z^h(k,z,t_0)=0$. Dark and black shades indicate the spatiospectral kinetic trench burnt by the optical field via stimulated emission. The light gray and white areas centered around $k\approx 6.5a_0^{-1}$ and $k\approx 7.5a_0^{-1}$ for the electron and holes, respectively, represent the spatiospectral distribution of the heated nonequilibrium carriers at the instant $t_0$.

curve of the generation rate shown in Fig. 5. With sufficient injection current applied to the laser, the injection of an optical beam leads to recombination of electron-hole pairs by stimulated emission of radiation. The closer the momenta of an electron-hole pair are to the peak of the generation-rate curve, the stronger the recombination will be. As the optical field shows strong spatiotemporal variations, a both spatially and spectrally confined hole is burnt into the dynamic carrier distributions.

#### *1. Effects of counterpropagation*

Figure 7(a) shows a snapshot of the dependence of the Wigner distribution $\delta f_z^e(k,z,t)=f^e(k,0,z,t)-f_{\mathrm{eq}}^e(k,0,z,t)$ on the wave number $k$ and the longitudinal position $z$ in the center $x=0$ of the broad-area laser. Gray shades correspond to $\delta f^e=0$. The nonequilibrium distribution of holes $\delta f_z^h(k,z,t)=f^h(k,0,z,t)-f_{\mathrm{eq}}^h(k,0,z,t)$ is displayed in Fig. 7(b). The darker the gray shades, the deeper the depletion of

the carrier distribution. In correspondence to the typical intensity distribution showing the amplification of the injected optical beam (e.g., Fig. 2), the depth of the kinetic trench burnt by the optical field increases longitudinally from $z=0$ to $z=L$. Its width is related to the linewidth of the optical transition and is determined by the microscopic carrier-carrier and carrier-phonon scattering processes represented by the time and space dependent relaxation rate distribution $\tau_p^{-1}(k,N,\mathbf{r},t)$.

But it is not only a spectral depletion of the carrier distribution functions between $ka_0 \approx 3.5$ and $ka_0 \approx 5$ which is caused by stimulated recombination: At the same time the optical field locally heats the electron and the hole plasma. Next to the black valley in Fig. 7 the spectrally and spatially confined accumulation of carriers (lightly shaded and white areas) indicates that electrons and holes are excited to nonequilibrium spatiotemporal states of high momentum. The carriers in these states locally have a higher momentum than the ones at quasiequilibrium. We recall that additionally, the spectral as well as the spatial position of the ''holes'' constantly varies in time.

Figure 7 clearly demonstrates that the maximum and the width of this absorption area are different for electrons and holes. This is due to a combination of a number of effects: First, the difference in band structure between the valence band and the conduction band is included via the effective masses of the electrons and the holes. Second, the corresponding differences in carrier mobilities appear in different amplitudes of the variations $\delta f_z^e(k,z,t)$ and $\delta f_z^h(k,z,t)$ for the carrier depletion and the carrier excitation. Third, the transfer of the carriers into states of higher momentum occurs via various carrier-phonon and phonon-phonon interactions [Eqs. (10) and (28)] with different relaxation rates for electrons and holes.

#### *2. Transverse filamentation*

From the snapshots of the intracavity intensity distribution (cf. Fig. 2) we have seen that the distribution of the optical intensity within the active zone is both longitudinally and transversely structured. In particular, the transverse structure exhibits a characteristic irregular modulation showing the formation of multiple transverse filaments. Due to the increased peak intensity values at the outcoupling facet, the modulation in the carrier density distribution and the spatial structure of the temperature is more pronounced (cf. Fig. 3). Both effects promote the formation of optical filaments. But it is not only in the spatial domain where the filamentation process is apparent. Figure 8, displaying a snapshot of the dependence of (a) the electron and (b) the hole Wigner distribution $\delta f_x^{e,h}(k,x,t)=f^{e,h}(k,L,x,t)-f_{\mathrm{eq}}^{e,h}(k,L,x,t)$ on the wave number $k$ and the transverse position $x$, respectively, illustrates the simultaneously occurring spectrally and spatially selective depletion (black) and nonequilibrium band filling processes. Again, the characteristic shape of the electron distributions [Fig. 7(a) and Fig. 8(a)] differ in both spectral position and magnitude of depletion and nonequilibrium filling from the corresponding hole distributions [Fig. 7(b) and Fig. 8(b)].

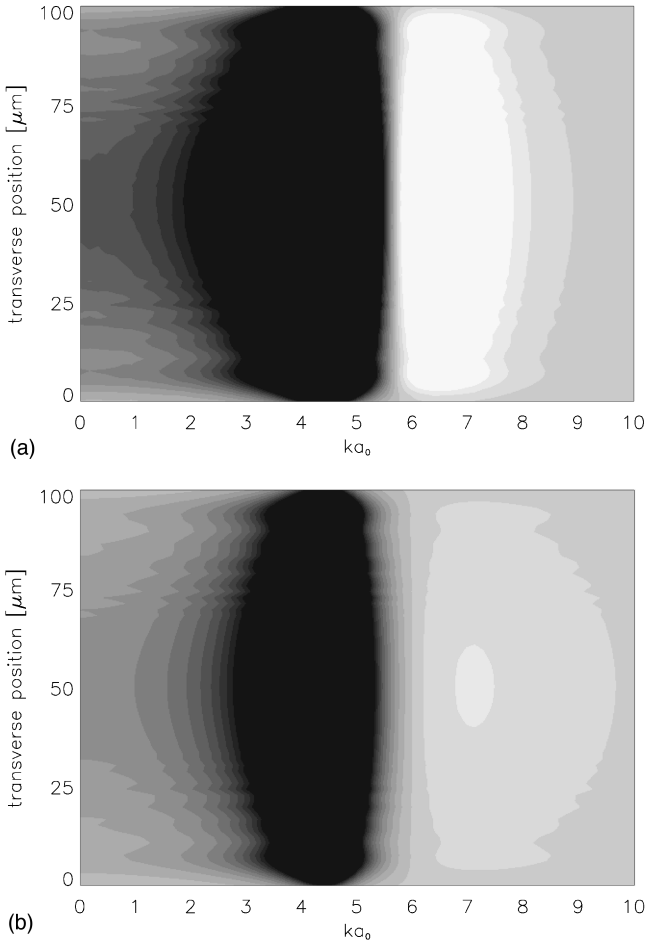


FIG. 8. Snapshots of the transverse structure of the nonequilibrium carrier Wigner distributions (a) $\delta f_x^e(k,x,t_0)$ and (b) $\delta f_x^h(k,x,t_0)$ at the outcoupling facet of the broad-area laser visualizing the spatiospectral nature of filamentation. Shading and the time $t_0$ correspond to the snapshots displayed in Fig. 7. Note again the difference in the spatiospectral location of the kinetic trench and the nonequilibrium heated states.

### C. Nonresonant excitation

Up to now, the excitation of the active semiconductor laser medium has been at resonance with the wavelength of the injected laser beam $\lambda_{\mathrm{inj}}$ corresponding to the wavelength $\lambda$ of the main laser mode. Starting from an equilibrium condition, the nonequilibrium carrier Wigner distributions directly reflect the internal length scales and dynamics of the active semiconductor medium. Any nonresonant excitation ($\lambda_{\mathrm{inj}} \neq \lambda$) should therefore change this situation. The nonequilibrium Wigner distributions do indeed reflect the dependence of the carrier depletion and heating on $\lambda_{\mathrm{inj}}$. Figures 9–11 show for three characteristic values of $\lambda_{\mathrm{inj}}$ snapshots of (a) the electron Wigner distribution $\delta f_z^e(k,z,t_0)$ in direct comparison with the corresponding spatiospectral Wigner distributions of (b) the real and (c) the imaginary parts of the interband polarization $p_z'(k,z,t_0)$ and $p_z''(k,z,t_0)$, respectively.

In Fig. 9 the wavelength of the injected beam has been set to 815 nm, the maximum of the gain bandwidth of the laser. As expected, the spectral depletion of the carrier distribution is very high and the kinetic trench is mostly confined to the

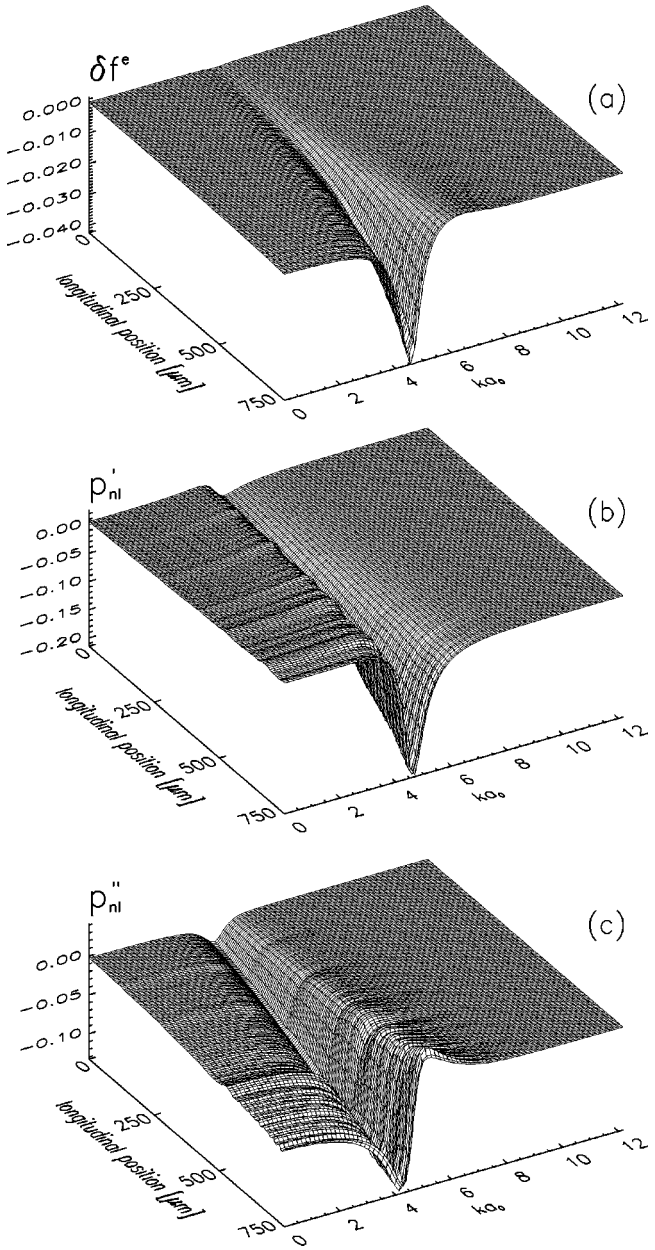


FIG. 9. Snapshots of the nonequilibrium Wigner distributions of (a) electrons $\delta f_x^e(k,x,t_0)$, (b) the real part of the interband polarization $p_z'(k,z,t_0)$, and (c) the imaginary part of the interband polarization $p_z''(k,z,t_0)$. The injection of the optical beam into the active layer of the broad-area laser occurs at resonance with $\lambda_{inj}=\lambda=815$ nm.

gain maximum. The snapshots of (a) $\delta f_z^e(k,z,t_0)$, (b) $p_z'(k,z,t_0)$, and (c) $p_z''(k,z,t_0)$ displayed in Fig. 9 illustrate the situation where the beam has, after a number of passes at $t_0\sim 50$ ps, significantly interacted with the active medium. In particular, while ''burning its trench'' within the cavity the input signal does not propagate unaffectedly. It is constantly modified and eventually its shape is spatially structured due to the interplay of absorption, carrier diffusion, diffraction, as well as relaxation of the light field and relaxation due to the carrier-phonon interaction. In Fig. 9(a) the shape of the kinetic trench is considerably smoother than both the real [Fig. 9(b)] and imaginary [Fig. 9(c)] part of the interband polarization. In the polarization, longitudinal structures appear on length scales which span a regime from 10 $\mu$m to 100 $\mu$m. These nonlinear structures reflect the density dependent microscopic relaxation of the polarization [4] which due to the propagation of the optical beam is directly transformed to a characteristic length scale. Consequently, the microscopic spatiospectral dynamics of the interband polarization being governed by the fast carrier-carrier and, in particular, by the carrier-optical phonon scattering processes determine both spectral and spatial scales of the light-matter interaction within the active area: It is these modulations in the polarization which are the seeds of the longitudinal variance of the intensity distribution (see Fig. 2) and which lead in combination with the spatiotemporal variation of the carrier density to the nonstationary spatiotemporal dynamics of the broad-area laser.

The combined spatial and spectral variation of the interband polarization displayed in Figs. 9(b) and 9(c) demonstrates the influence of the microscopic spatiospectral dynamics on the nonlinear gain (cf. Fig. 5) and refractive index (cf. Fig. 6) variations. The real part of the nonlinear polarization shown in Fig. 9(b) visualizes the spectral dependence and longitudinal variation of the generation rate and thus the spatiospectral distribution of the optical gain. Note that in Fig. 9(b) negative values of $p_z'(k,z,t_0)$ represent positive local gain. The corresponding spatial variation of the dispersion of the nonlinear induced refractive index $\delta n$ can on the other hand directly be deduced from the $k$ dependence of $p_z''(k,z,t_0)$ [Fig. 9(c)]. Noting that generally $-\delta n\sim p_z''$, the longitudinal shape of $p_z''(k,z,t_0)$ [Fig. 9(c)] reveals the density dependence of the induced nonlinear refractive index. The optical beam which is injected constantly gains in amplitude and thus leads to a rising depletion of the density of charge carriers. This, in turn, causes an increase of the refractive index within the cavity from $z=0$ to $z=L$.

The dependence on $\lambda_{inj}$ becomes apparent when comparing Fig. 9 with Fig. 10 and Fig. 11, where $\lambda_{inj}$ is 815 nm, 795 nm, and 765 nm, respectively. Figure 10 thus demonstrates the change in the behavior of the broad-area laser when using a nonresonant input beam of shorter wavelength: As the input beam determines the progression and the position of the kinetic trench in the generation rate, a shift of $\lambda_{inj}$ towards shorter wavelengths results in a corresponding spectral drift of all Wigner distributions. In particular, Fig. 10(b) pertains to the conditions where $p_z'(k,z,t_0)$ is about to change from net gain to net absorption. In this case, a spectral shift of the minimum of the generation rate $\delta f_z^e(k,z,t_0)$ from $k\sim 4a_0^{-1}$ at resonance [Fig. 9(a)] to $k\sim 5.5a_0^{-1}$ at $\lambda_{inj}=795$ nm is clearly visible. However, Figs. 9(a) and 9(b) also demonstrate that a wavelength detuning $\Delta\lambda=\lambda-\lambda_{inj}=20$ nm causes a balance of net gain and net absorption but is not yet sufficiently large to create significantly heated nonequilibrium carrier distributions. Moreover, Figs. 9(b) and 9(c) reveal that in propagation direction of the optical beam a frequency shift of the resonance frequency towards smaller values of the wave number $k$ occurs together with a broadening of the line shape. This is in contrast to the case of the strong nonresonant excitation pertaining to Fig. 11(c) where the frequency shifts in opposite direction towards larger wave numbers.

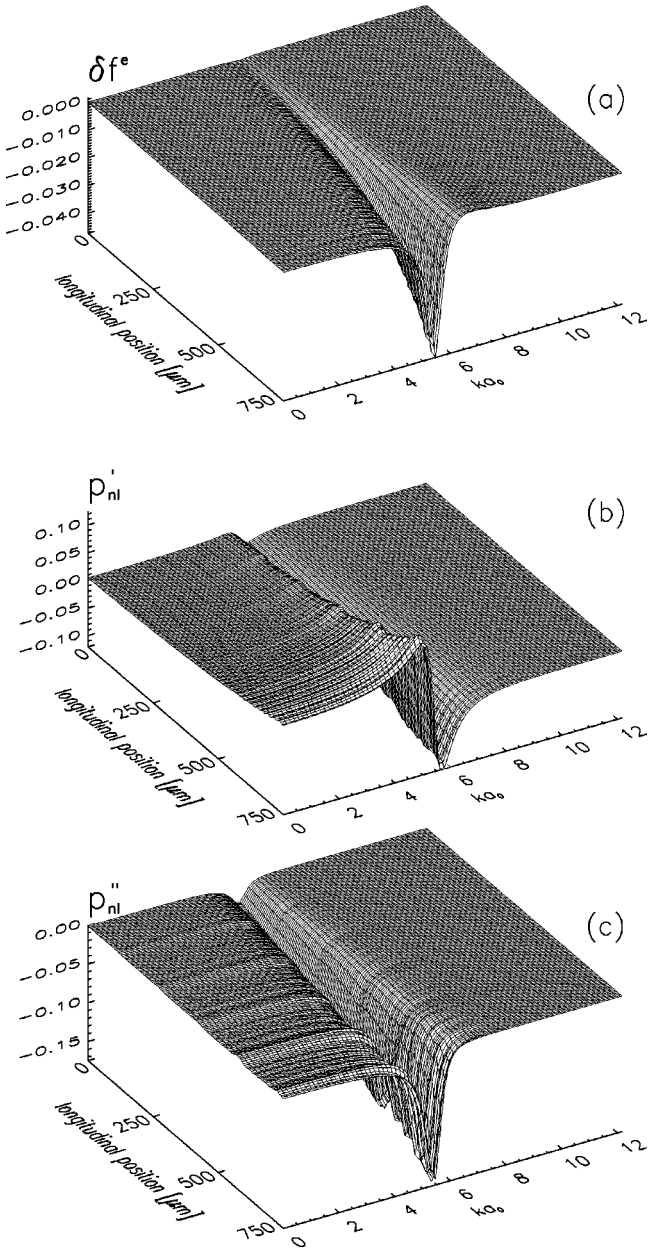


FIG. 10. Nonresonant excitation of the broad-area semiconductor laser with $\lambda_{inj}=795$ nm representing a wavelength detuning $\delta\lambda=20$ $\mu$m. The individual plots represent snapshots of the nonequilibrium Wigner distributions of (a) electrons $\delta f_x^e(k,x,t_0)$, (b) the real part of the interband polarization $p_z'(k,z,t_0)$, and (c) the imaginary part of the interband polarization $p_z''(k,z,t_0)$.

With increasing wavelength detuning, Fig. 10 and Fig. 11 show that the carrier heating effects gain influence while at the same time the carrier depletion by stimulated emission is reduced: Fewer and fewer electron-hole pairs are locally available at momentum states (wavelengths) suitable for recombination. Thus, with decreasing wavelength, the real and the imaginary part of the interband polarization [Figs. 10(b) and 10(c)] change their sign towards absorption.

In the case of strong detuning a number of characteristic nonequilibrium effects can be observed in the Wigner distributions shown in Fig. 11. First, the nonresonant excitation generates during propagation of the optical beam with $\lambda_{inj}=765$ nm in the carrier Wigner distribution $\delta f^e$ [Fig. 11(a)]

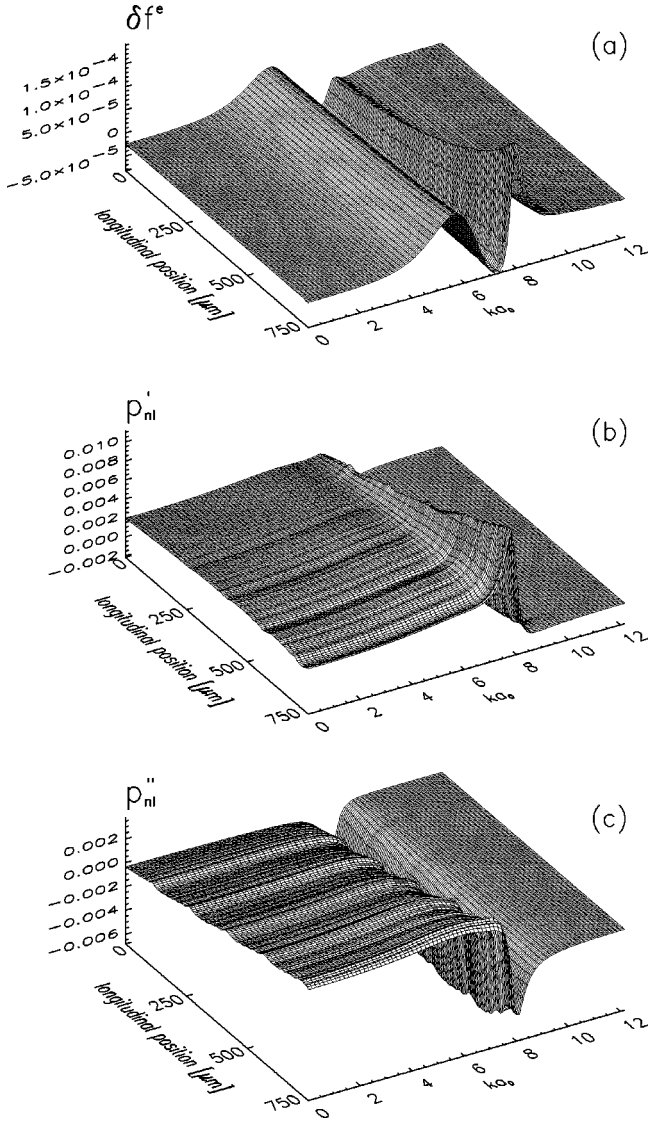


FIG. 11. Nonequilibrium Wigner distributions at strongly nonresonant excitation ($\lambda_{inj}=765$ nm). (a) Electron Wigner distribution $\delta f_x^e(k,x,t_0)$. (b) and (c) show the real $[p_z'(k,z,t_0)]$ and imaginary $[p_z''(k,z,t_0)]$ parts of the Wigner distribution of the interband polarization.

a longitudinally increasing but spectrally well-confined density of nonequilibrium states at $k\sim 8a_0^{-1}$. After this excitation, the coupling to the longitudinal optical phonons leads to the situation depicted in Fig. 11(a) where a significant proportion of carriers has accumulated in the heated nonequilibrium states at $k\sim 6a_0^{-1}$. Stimulated recombination at resonance, however, is prevented by the particular distribution of the generation rate [Fig. 11(b)] and refractive index [Fig. 11(c)]. As a consequence, the laser adjusts its emission wavelength accordingly and the depletion of carriers takes place at wavelengths corresponding to $k\sim 7a_0^{-1}$. Again, the longitudinal modulations of $p_z'(k,z,t_0)$ and $p_z''(k,z,t_0)$ provide the explanation of the formation and persistence of the longitudinal structures of the optical field. Note in particular the high degree of regularity in the modulations in Fig. 11(c) which act as an induced macroscopic distributed feedback grating. This is in contrast to the resonant case where the

amplification of the beam leads to a significant and spatially structured reduction of the carrier density.

## V. CONCLUSION

We have discussed the spatiotemporal intensity and temperature dynamics and presented novel results on the spatiospectral dynamics of nonequilibrium carrier Wigner distributions of broad-area semiconductor lasers. The spatiospectral excitation and relaxation dynamics represented by the nonequilibrium carrier Wigner distributions are included in the microscopic numerical simulation. The simulations are based on an extension of the Maxwell-Bloch equations for spatially inhomogeneous semiconductor laser structures by combining them in a self-consistent way with equations describing ambipolar carrier transport and relaxation of the energy densities of electrons and holes.

Characteristic and representative snapshots of the carrier Wigner distributions (Fig. 7 and Fig. 8) show in combination with images of the spatiotemporal variation of the intensity, carrier density, refractive index, and carrier plasma temperatures (Fig. 2 and Fig. 3) that in the broad-area laser the nonequilibrium Wigner distributions of the charge carriers and the polarization vary in time, space, and momentum in a complex fashion. Via the characteristic carrier-carrier and carrier-phonon scattering processes on the one hand and carrier heating and phononic relaxation effects on the other hand, the phenomena of dynamic spatiospectral hole burning and nonequilibrium band filling are intrinsically coupled. Consequently, in semiconductor lasers and amplifiers with a characteristically wide- and long-gain region such as the broad-area laser, the combination of spectral and spatial excitation, relaxation, and transport processes determines their spatiotemporal dynamics. It is vividly characterized by nonequilibrium spatiotemporal structures in the joint time-space-momentum phase space represented by snapshots of the nonequilibrium Wigner distributions. We have identified the various microscopic processes which determine the spatial and spectral characteristics of the broad-area laser under resonant and nonresonant optical excitation. On the other hand, it has been demonstrated that the macroscopic device architecture strongly influences the processes occurring on microscopic scales. Explicitly taking the device structure into account in the simulations, the spatiospectral nonequilibrium dynamics of the Wigner distributions, indeed, represent an actual experimental situation. With proper adjustment of the device parameters (cavity length, width of active zone, etc.) our theoretical simulations should therefore allow direct comparison with experiments. Thus knowledge about the macroscopic appearance of the spontaneous formation of nonequilibrium structures in the Wigner distributions of the carriers and interband polarization may be at the same time of fundamental significance and relevant for the design of novel devices.

## ACKNOWLEDGMENT

We would like to thank Professor R. Wallenstein for his interest and continuing support.

[1] *Diode-Laser Arrays*, edited by D. Botez and D. R. S. (Cambridge University Press, Cambridge, England, 1994).
[2] O. Hess and T. Kuhn, Prog. Quantum Electron. **20**, 85 (1996).
[3] O. Hess, Chaos Solitons Fractals **4**, 1597 (1994).
[4] O. Hess and T. Kuhn, Phys. Rev. A **54**, 3347 (1996).
[5] O. Hess and T. Kuhn, Phys. Rev. A **54**, 3360 (1996).
[6] I. Fischer, O. Hess, W. Elsäßer, and E. Göbel, Europhys. Lett. **35**, 579 (1996).
[7] C. M. Bowden and G. P. Agrawal, Phys. Rev. A **51**, 4132 (1995).
[8] J. Yao, G. P. Agrawal, P. Gallion, and C. M. Bowden, Opt. Commun. **119**, 246 (1995).
[9] S. Balle, Opt. Commun. **119**, 227 (1995).
[10] F. Jahnke and S. W. Koch, Opt. Lett. **18**, 1438 (1993).
[11] A. Knorr, R. Binder, E. M. Wright, and S. W. Koch, Opt. Lett. **18**, 1538 (1993).
[12] R. A. Indik *et al.*, J. Opt. Soc. Am. B **14**, 754 (1997).
[13] F. Jahnke and S. W. Koch, Phys. Rev. A **52**, 1712 (1995).
[14] S. Hughes, A. Knorr, and S. W. Koch, J. Opt. Soc. Am. B **14**, 754 (1997).
[15] W. W. Chow, S. W. Koch, and M. S. III, *Semiconductor-Laser Physics* (Springer-Verlag, Berlin, 1994).
[16] T. Held, T. Kuhn, and G. Mahler, Phys. Rev. B **44**, 12 873 (1991).
[17] C. Z. Ning, R. A. Indik, and J. V. Moloney, J. Opt. Soc. Am. B **12**, 1993 (1995).
[18] C.-Y. Tsai, C.-Y. Tsai, R. M. Spencer, and Y.-H. Lo, IEEE J. Quantum Electron. **32**, 201 (1996).
[19] W. Pötz and P. Kocevar, in *Hot Carriers in Semiconductor Nanostructures*, edited by C. Weisbuch and E. Burnstein (Plenum Press, New York, 1992), pp. 87–120.
[20] S. Adachi, J. Appl. Phys. **58**, R1 (1985).
[21] Y. P. Varshni, Physica **34**, 149 (1967).
[22] R. Zimmermann, Phys. Status Solidi B **146**, 371 (1988).
[23] T. Kuhn and G. Mahler, Solid-State Electron. **32**, 1851 (1989).
[24] H. Hillmer *et al.*, Opt. Quantum Electron. **26**, S691 (1994).
[25] G. H. B. Thompson, *Physics of Semiconductor Laser Devices* (Wiley, New York, 1980).
[26] I. S. Grieg and J. D. Morris, J. Comput. Phys. **20**, 60 (1976).
[27] W. H. Press, B. P. Flannery, S. A. Teukolsky, and W. T. Vetterling, *Numerical Recipes* (Cambridge University Press, Cambridge, England, 1989).
[28] G. P. Agrawal and N. K. Dutta, *Long-Wavelength Semiconductor Lasers* (Van Nostrand Reinhold, New York, 1986).